ACS OMEGA

http://pubs.acs.org/journal/acsodf

Article

Effect of Calcination Temperature on Cu-Modified Ni Catalysts Supported on Mesocellular Silica for Methane Decomposition

Orrakanya Phichairatanaphong, Yingyot Poo-Arporn, Metta Chareonpanich, and Waleeporn Donphai*

Cite This: *ACS Omega* 2022, 7, 14264−14275

Read Online

ACCESS | Metrics & More | Article Recommendations | Supporting Information

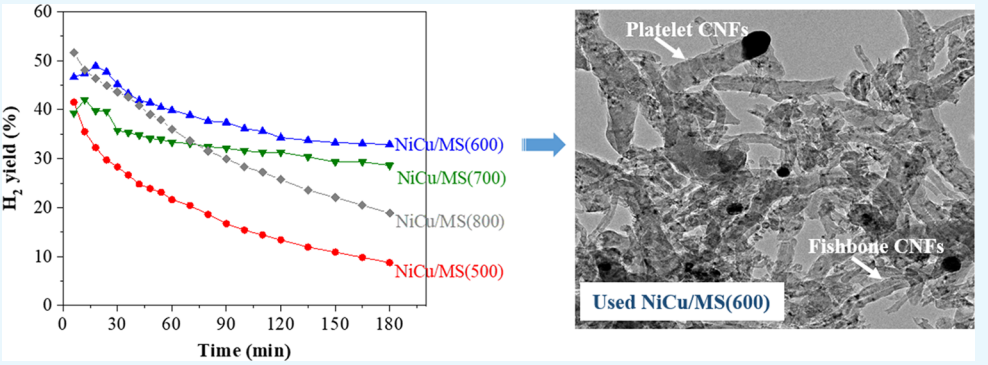

ABSTRACT: Catalytic methane decomposition has been considered suitable for the green and sustainable production of high-purity H_2 to help reduce greenhouse gas emissions. This research developed a copper-modified nickel-supported mesocellular silica NiCu/MS(x) catalyst synthesized at different calcination temperatures to improve the activity and stability in the CH_4 decomposition reaction at 600 °C. Ni and Cu metals were loaded on a mesocellular silica (MS) support using a co-impregnation method and calcined at different temperatures (500, 600, 700, and 800 °C). The NiCu/MS(600) catalyst not only had the highest H_2 yield (32.78%), which was 1.47−3.87 times higher than those of the other NiCu/MS(x) catalysts, but also showed better stability during the reaction. Calcination at 600 °C helps improve the active nickel dispersion, the reducibility of the NiCu catalyst, and the interaction of the NiCu−MS support, leading to the formation of fishbone and platelet carbon nanofibers via a tip-growth mechanism, resulting in the NiCu metals remaining active during the reaction.

1. INTRODUCTION

Hydrogen (H_2) gas has been considered as one of the key energy carriers and a key fuel for the 21st century, as it not only shows great potential in a wide variety of industrial applications but can also reduce environmental impacts.[1−3] H_2 has been widely used in the chemical process industry, electronics, and food processing.[3−5] At present, a large-scale hydrogen production is based on methane steam reforming (MSR) and partial oxidation of methane (POM). In MSR and POM reactions, carbon dioxide (CO_2) and carbon monoxide (CO) are simultaneously produced during the processes.[6−8] Therefore, these processes are not environmentally friendly, as they need considerable investment in both equipment and energy consumption to separate the CO_2 and CO from the H_2.

Catalytic methane decomposition is a green and sustainable process that is consistent with reducing greenhouse gas emission because a methane molecule is directly decomposed to COx-free H_2 and carbon filament products.[2,3,9−13] Carbon filaments, such as carbon nanofibers and carbon nanotubes produced through this process have been widely used in many industrial applications, including functional materials, catalysts, hydrogen storage, and electrodes.[14−16] Catalytic methane decomposition can occur in a relatively lower temperature range compared to MSR and POM reactions.[3,4] However, breaking the methane molecule requires a lot of energy (high temperature) due to its symmetrical structure and the strong C−H bond (440 kJ/mol). Therefore, the use of an appropriate metal catalyst is necessary. Non-novel transition metals, such as nickel (Ni), cobalt (Co), and iron (Fe), have been reported to be active in methane decomposition due to their common, unique property of partly filled 3d orbitals.[2,17,18] In particular, a Ni catalyst is highly active at low reaction temperatures (500−600 °C) compared to the other catalysts because it has the greatest decrease in the dissociation energy of the C−H bonds;[2−4] however, a Ni-based catalyst is easily deactivated by the sintering effect at a higher temperature (greater than 600

Received: February 19, 2022
Accepted: April 6, 2022
Published: April 14, 2022

Table 1. Textural and Chemical Properties of NiCu/MS(x) Catalysts

catalysts	surface area (m^2/g)	pore diameter (nm)	pore volume (cm^3/g)	metallic Ni crystalline[a] size (nm)	active Ni surface area[b] (m^2/g_{metal})
NiCu/MS(500)	181	3.70, 6.76	0.28	39.8	0.083
NiCu/MS(600)	164	3.71, 6.77	0.25	35.4	0.052
NiCu/MS(700)	141	3.70, 6.77	0.25	37.3	0.024
NiCu/MS(800)	88	3.70, 7.37	0.20	36.6	0.022

[a]Calculated from the Scherrer equation. [b]Calculated based on CO pulse chemisorption.

°C) and by carbon encapsulation, resulting in lower catalytic activity during the reaction.[3,4,19]

Notably, the activity and stability of a Ni-based catalyst can be improved by selecting suitable supports and promoters because these supports have a substantial role in the catalytic reaction as they help to increase the metal catalyst dispersion and therefore, improve the activity of catalysts while minimizing the catalyst sintering. Many types of materials such as silica[20−23] (SiO_2), alumina[21] (Al_2O_3), zeolite,[21] and metal oxides,[21,23−25] such as ZrO_2, MgO, and TiO_2, have been used as catalyst supports for catalytic methane decomposition. SiO_2 material has been widely used as support because the interaction between metal and silica support is quite weak compared to the other supports in which the metal−support interaction is one of the factors determining the activity and lifetime of the catalyst.[3,4,22] Our previous work found that the SiO_2 structure support directly affected activity and stability in the methane decomposition reaction. Ni supported on bimodal porous silica with mesopore and macropore structures produced higher activity and stability than that of Ni supported on monomodal porous silica with straight and sinusoidal mesopore[26] because a larger pore size of the support enhanced the diffusion of the reactant gas during the reaction. However, the activity of catalysts with a larger pore size still decreased gradually during the reaction due to their lower active metal dispersion.[26] Mesocellular silica (MS) is a type of porous silica that has a 3D structure with ultralarge (15−50 nm) pore diameters that are accessible via large windows (5−20 nm). In addition, the pore characteristic of MS can be controlled depending on the synthesis conditions. The MS structure has the advantage of better diffusion of the reactant for its 3D continuous mesopore system and interconnected windows.[27,28] Hence, MS material is of interest for use as a catalyst support.

The addition of a promoter metal can help to enhance the metal-catalyst dispersion and reducibility, assuring improving catalyst activity and simultaneously prolonging the catalyst's lifetime during the reaction. Various types of metals such as Cu, Pt, Pd, Fe, Co, and Mo, have been used as a promoter for catalyst methane decomposition.[3,4] In particular, Cu metal has the greatest potential as a Ni-based catalyst. Many researchers have reported the effect of bimetallic NiCu supported on different types of supports, including Al_2O_3, MgO, $MgO{\cdot}Al_2O_3$, MCM-41, SiO_2, and CNTs in the CH_4 decomposition reaction.[2,14,17,29−33] It was found that the addition of Cu could noticeably enhance catalytic stability compared to the monometallic Ni catalyst because Cu could improve the metal dispersion and reducibility of the nickel catalyst.[14,17,25,33] In addition, the Ni−Cu alloy is notable for enhancing the stability and activity of the catalyst at high temperatures; furthermore, it promotes the carbon formation rate because of favoring carbon diffusion through the higher lattice constant of the NiCu alloys.[30−32] However, the NiCu catalyst was still deactivated during the methane decomposition reaction.

Therefore, this research developed Ni−Cu supported mesocellular silica [NiCu/MS(x)] catalysts synthesized at different calcination temperatures to improve the activity and stability in the CH_4 decomposition reaction at 600 °C. The effect of calcination temperature (500, 600, 700, and 800 °C) on the structural and chemical surface properties of Ni and Cu species on hydrogen production, carbon product allotrope, and the deactivation behaviors of NiCu/MS(x) catalysts were discussed in detail. It was found that the NiCu/MS(x) catalyst calcined at 600 °C produced the highest CH_4 conversion and H_2 yield; concurrently, the activity was stable during the reaction. The calcination temperature significantly affected the reduction behavior of the NiCu catalyst, active metal dispersion, and the interaction of the Ni and MS support, directly resulting in the decomposition of CH_4 to H_2, and the formation of carbon nanofibers (CNFs), as well as deactivation of the catalyst.

2. RESULTS AND DISCUSSION

2.1. Structural and Chemical Surface Properties of NiCu/MS(x) Catalysts. The textural properties of the nitrogen adsorption−desorption isotherms and pore size distributions of NiCu/MS(x) catalysts are shown in Figure S1. All NiCu/MS(x) catalysts had the type IV isotherm with an H3 hysteresis loop, indicating the presence of a mesoporous structure with aggregated, plate-like particles consisting of macropores that were not completely filled with pore condensate.[34] As shown in Figure S1B, each NiCu/MS(x) catalyst had two small mesopore sizes at the main peaks of 3.71 and 6.78 nm, with a larger mesopore size at the main peak of 45 nm; however, the pore size at the peak intensities of 6.78 and 45 nm decreased when the calcination temperature increased. The specific surface area, pore size, and pore volume of catalysts are reported in Table 1. With the increase in calcination temperature, the specific surface area and pore volume tended to decrease because the nickel−copper particles easily agglomerated into larger particle size and blocked the MS support pores.

The structures of the NiCu/MS(x) catalysts and the nickel and copper dispersions on the MS support calcined using different temperatures were observed using the TEM technique. Figure S2a,c focused on the MS support structure; a foam-like structure was found in all catalysts, with this structure comprising various-sized interconnected spherical cells.[35] The size and dispersion (Figure 1) of nickel oxide and copper oxide consisted of NiO nanoparticle sizes of NiCu/MS(500), NiCu/MS(600), NiCu/MS(700), and NiCu/MS(800) in the ranges 11.2−47.0, 5.1−37.7, 14.6−55.0, and 8.0−42.9 nm, respectively. The nickel−metal was well dispersed on the MS support in all NiCu/MS(x) catalysts. At higher calcination temperature, the larger NiO particle size located at the edge and on the external surface of the MS support.

https://doi.org/10.1021/acsomega.2c01016
ACS Omega 2022, 7, 14264−14275

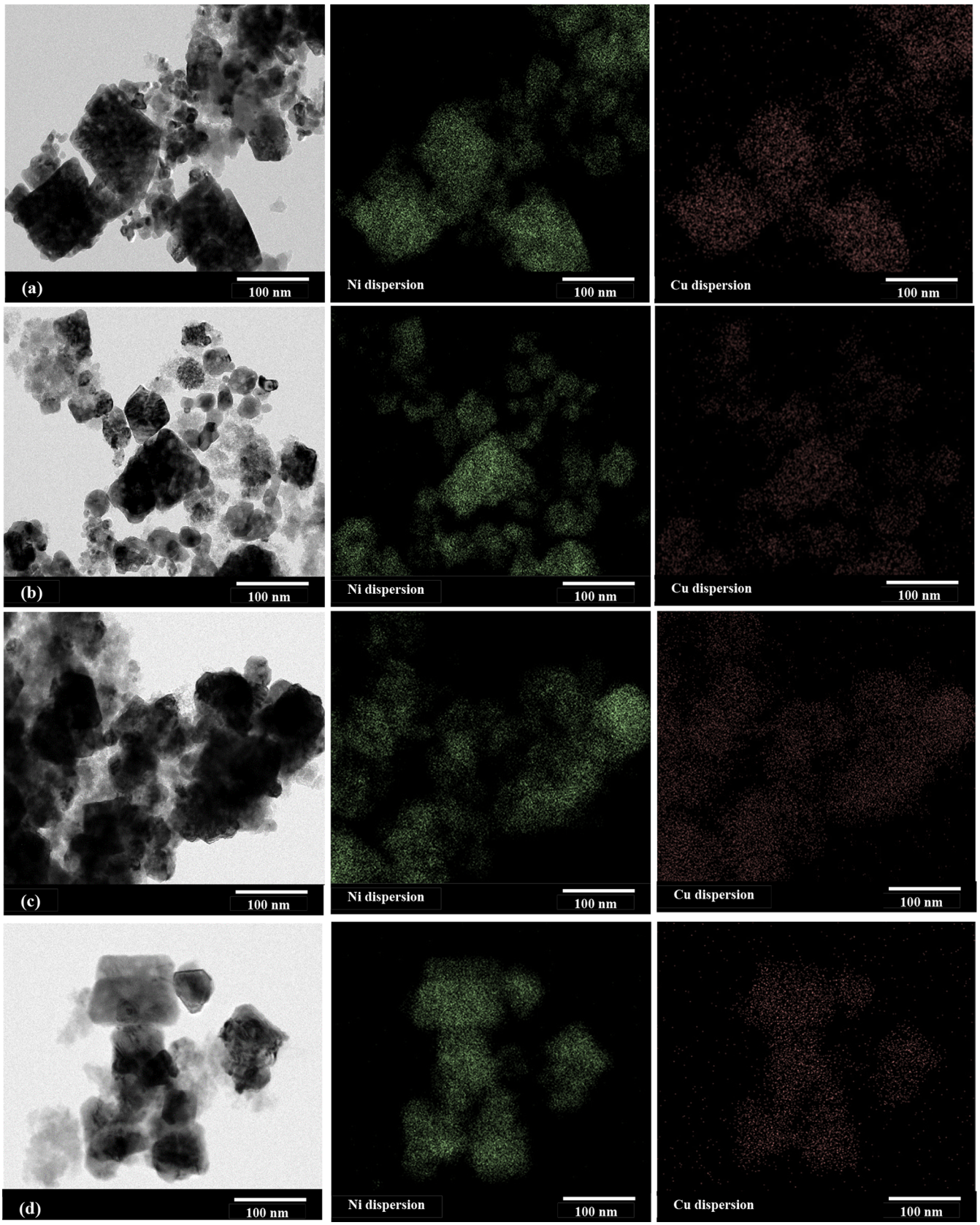

Figure 1. TEM image and EDS-mapping of nickel and copper in the NiCu/MS catalyst calcined at different temperatures. (a) NiCu/MS(500), (b) NiCu/MS(600), (c) NiCu/MS(700), and (d) NiCu/MS(800).

The particle size of CuO could not be measured because the amount of copper loading (5 wt %) was quite low compared to the nickel loading (50 wt %). However, the copper metal was well dispersed on the NiCu/MS catalyst.

https://doi.org/10.1021/acsomega.2c01016
ACS Omega 2022, 7, 14264−14275

The reduction temperature and interaction between nickel, copper, and the MS support of Ni−Cu/MS(x) catalysts calcined at different temperatures were analyzed using the H_2-temperature-programmed reduction (H_2-TPR) technique, as shown in Figure 2. All NiCu/MS(x) catalysts had three

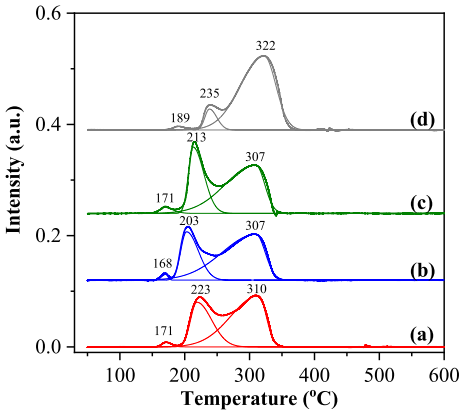

Figure 2. H_2-TPR profiles of fresh NiCu/MS(x) catalysts. (a) NiCu/MS(500), (b) NiCu/MS(600), (c) NiCu/MS(700), and (d) NiCu/MS(800).

reduction peaks. The first region in the range 70−190 °C was attributed to reduction of the CuO phase to metallic copper (Cu^0).[2,14] The second region in the range 190−260 °C corresponded to the reduction of bulk NiO on the MS support.[2,25] In this region, the reduction peak of the NiCu/MS(600) catalyst shifted to a lower reduction temperature due to the smaller size of its nickel oxides on the surface. The last reduction range of 260−350 °C indicated the reduction of NiO that strongly interacted with the MS support.[2,29] In our previous work,[36] the reduction temperatures of monometallic Ni loaded on the silica support were in the range 400−600 °C, implying that nickel strongly interacted with the silica support. The addition of Cu into the Ni catalyst could facilitate the reducibility of NiO at a lower temperature through the adsorption of hydrogen on copper oxide.[14,37] Furthermore, the calcination temperature affected the interaction between Ni−Cu and the MS support. At calcination temperatures of 500 and 800 °C, the interactions between Ni−Cu and MS support were much stronger compared to the catalysts calcined at 600 and 700 °C.

The effect of the calcination temperature on the phase transformation of the nickel metal on the NiCu/MS(x) catalyst during the reduction process was proved using in situ X-ray absorption near edge structure (XANES) spectroscopy. The normalized Ni K-edge XANES spectra of each catalyst compared with the spectrum of NiO and Ni foil (metallic Ni) standards are presented in Figure 3A. The nickel species of all calcined NiCu/MS catalysts was the NiO phase. The NiO phase was slightly changed to metallic nickel during the reduction process under a hydrogen atmosphere. The NiO on NiCu/MS(600) catalyst began to change to metallic nickel species at a lower temperature compared to those of the NiCu/MS(x) catalysts due to the weaker interaction of Ni and the MS surface (confirmed by the H_2-TPR data, Figure 2). After the catalyst had been reduced using hydrogen gas at 700 °C for 1.5 h, the NiO metal was completely changed to metallic nickel (Ni^0) as an active species in all NiCu/MS(x) catalysts.

The copper phases on the NiCu/MS(x) catalysts after the calcination process and after the reduction process at 700 °C with 90 min holding time were confirmed using in situ XANES spectroscopy, by comparing with each standard spectra of copper oxide and copper foil, as shown in Figure 4A,B, respectively. All the calcined NiCu/MS(x) catalysts had a white line peak at 8996.7 eV, which was the same as for the CuO standard spectra. After the reduction process, all the reduced NiCu/MS(x) catalysts had a pre-edge peak (8994.5 eV) and an edge jump (9003.3 eV) similar to those of metallic copper (Cu^0), showing that the CuO species on the fresh NiCu/MS(x) catalysts were completely changed to metallic copper prior to the methane decomposition reaction. The fine structure of the white line was slightly different due to the effect of copper particle size.[36]

The chemical states of nickel and copper on the reduced NiCu/MS(x) catalysts calcined at different temperatures were characterized in the binding energy regions of Ni $2p_{3/2}$ and Cu $2p_{3/2}$, as shown in Figure 5A,B, respectively. From the peak characteristics in the Ni $2p_{3/2}$ core level spectra, the peaks at 852.9 ± 0.3, 854.6 ± 0.2, and 856.2 ± 0.4 eV, corresponding to metallic nickel, NiO (Ni^{2+}), and $Ni(OH)_2$ (Ni^{2+}),[38,39] respectively, were found in all Ni−Cu/MS(x) catalysts. With the Cu $2p_{3/2}$ core level spectra, the XPS spectra of all NiCu/MS(x) catalysts were deconvoluted into three Gaussian peaks at 932.4 ± 0.6 and 934.3 ± 1.1 eV, ascribed to the reduced copper species (Cu^0/Cu^+) and CuO (Cu^{2+}),[40,41] respectively. NiO and CuO peaks were found in all reduced catalysts, probably due to unavoidable air oxidation of the catalyst during loading into the instrument. The binding energies of Ni 2p and Cu 2p of the reduced NiCu/MS(600) catalyst shifted lower, which could be explained by a charge transfer from Cu in close contact with Ni metal by means of a high portion of Ni−Cu alloy formation.[20] For the reduced NiCu/MS(700) and NiCu/MS(800) catalysts, the binding energies of Ni 2p and Cu 2p shifted higher, which could be explained by the charge compensation phenomenon of the binary NiCu-supported catalysts. Naghash et al. reported that at temperatures above 700 °C, the interfacial energy of copper and nickel was high; therefore, the copper and nickel atoms tended to segregate rather than be uniformly dispersed on the support surface.[42]

The metal crystalline phases of the reduced NiCu/MS(x) catalysts calcined at different temperatures were characterized using XRD measurements (Figure 6). All NiCu/MS(x) catalysts had four diffraction peaks. The diffraction peaks at 44.42° and 51.76° were assigned to the crystal planes (111) and (200) of the Ni−Cu alloy (JCPDS. 47-1406), respectively. The shoulders, which were located at 44.51° and 51.92° corresponded to the crystal planes (111) and (200) of the metallic nickel (JCPDS. 4-0850), respectively.[14,42,43] The diffraction peaks of copper were not found in any catalysts because the crystallite size of copper could be below the detection limit of the XRD technique (<5 nm). The crystallite size of metallic nickel on the NiCu/MS catalysts was calculated using the Scherrer equation and the result is presented in Table 1. The smallest and largest metallic nickel crystallite sizes were observed with the NiCu/MS(600) and NiCu/MS(500) catalysts, respectively.

The active surface area of nickel on the NiCu/MS(x) catalysts with different calcination temperatures after the reduction process with H_2 gas at 700 °C for 1.5 h was examined using a CO chemisorption technique; the results are

https://doi.org/10.1021/acsomega.2c01016
ACS Omega 2022, 7, 14264−14275

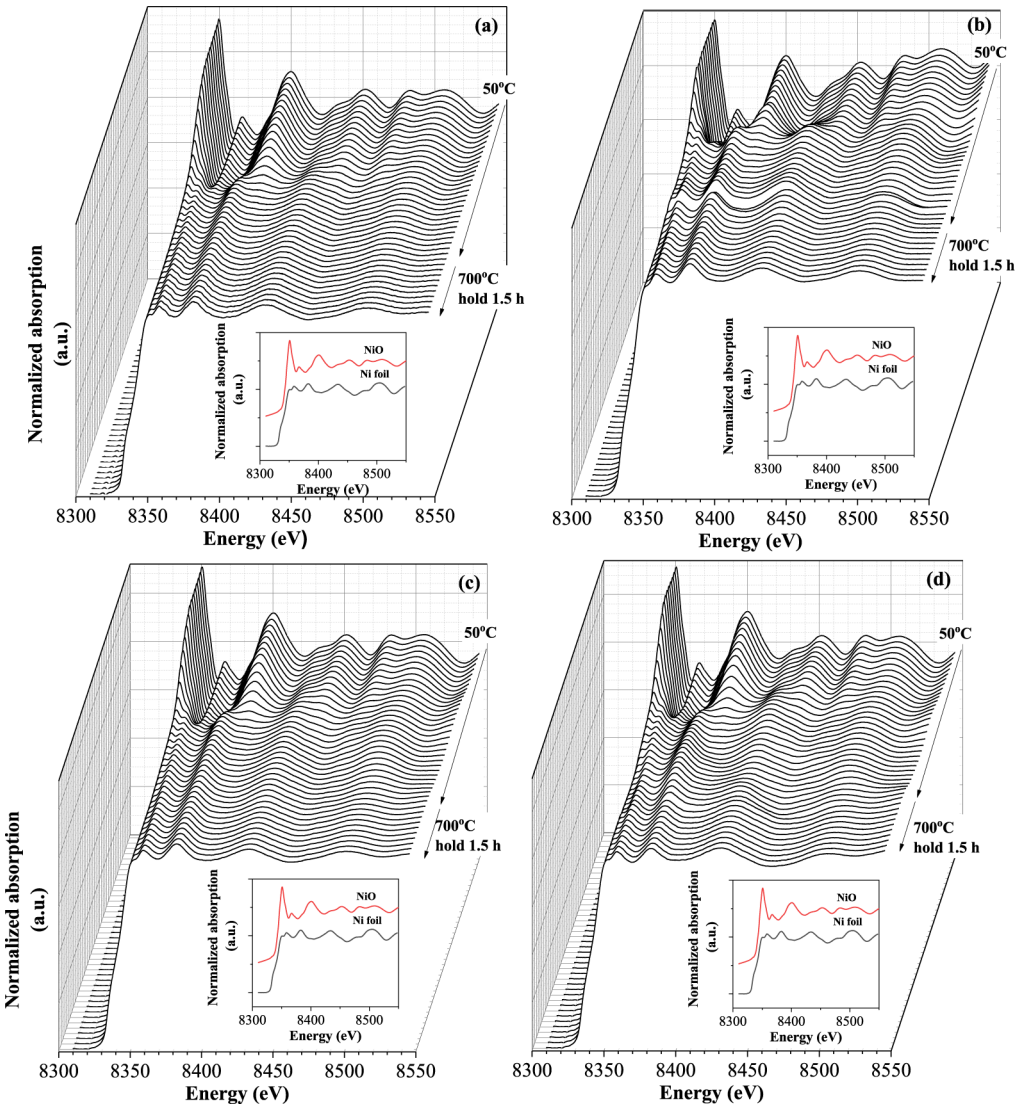

Figure 3. In situ Ni K-edge XANES spectra of fresh catalysts during the reduction process from 50 to 700 °C and 90 min holding time: (a) NiCu/MS(500), (b) NiCu/MS(600), (c) NiCu/MS(700), and (d) NiCu/MS(800). Inset shows spectra of nickel standards.

presented in Table 1. The highest and lowest nickel active surface areas were for NiCu/MS(500) (the lowest calcination temperature) and Ni−Cu/MS(800) catalyst (the highest calcination temperature), respectively, because the higher calcination temperature resulted in the agglomeration of nickel and copper metals of a larger size, and therefore, the active nickel surface area decreased.

The calcination temperature directly affected the structural and chemical properties of the NiCu/MS(x) catalysts in terms of nickel metal dispersion, a portion of Ni−Cu alloy formation, the reduction behavior of nickel, and NiCu−MS support interaction. A higher temperature resulted in higher interfacial energies of copper and nickel, resulting in the formation of nickel and copper clusters rather than the nickel−copper alloy phase on the support surface.

2.2. NiCu/MS(x) Catalyst Performance in Methane Decomposition. The effect of calcination temperature on the activity and stability of NiCu/MS(x) catalysts in methane decomposition was investigated at 600 °C under atmospheric pressure in a packed-bed reactor. The CH_4 conversion and H_2 yield of the NiCu/MS(x) catalysts calcined at different temperatures are shown in Figure 7a,b, respectively. The NiCu/MS(600) catalyst had the highest CH_4 conversion (58%) at commencement and the activity decreased to 40% conversion within 60 min and was quite stable until 3 h of reaction time. In addition, the NiCu/MS(600) catalyst had the highest H_2 yield. The NiCu/MS(800) catalyst had a higher CH_4 conversion and H_2 yield at reaction commencement, but its performance continuously decreased with the increase in reaction time and ultimately was lower than those of the NiCu/MS(600) and NiCu/MS(700) catalysts. The NiCu/MS(700) catalyst had higher activities in terms of CH_4 conversion and H_2 yield compared to the NiCu/MS(800) catalyst, especially during 60−180 min. The NiCu/MS(500) catalyst had the lowest CH_4 conversion and H_2 yield, as well catalyst activity being significantly deactivated during the reaction time.

At the end of the reaction period (180 min), NiCu/MS(600) catalyst produced H_2 gas expressed in terms of H_2 yield (approximately 32.78%) that was 3.87, 1.47, and 1.75 times higher than for the NiCu/MS(500), NiCu/MS(700), and NiCu/MS(800) catalysts, respectively. The amount of carbon on the NiCu/MS(x) catalysts was calculated based on the thermogravimetric analysis (TGA) data, as presented in

https://doi.org/10.1021/acsomega.2c01016
ACS Omega 2022, 7, 14264−14275

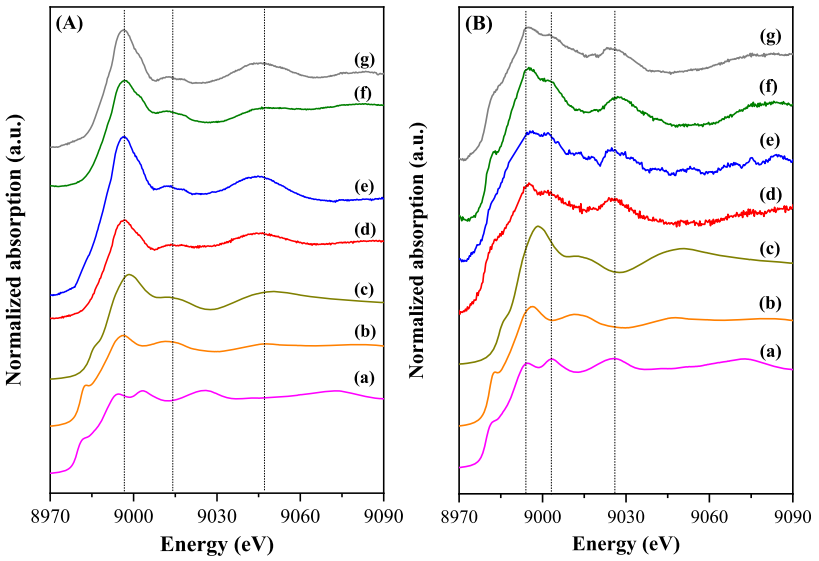

Figure 4. In situ Cu K-edge XANES spectrum of catalysts (A) after calcination process and (B) after reduction process at 700 °C and 90 min holding time: (a) Cu foil, (b) Cu_2O, (c) CuO, (d) NiCu/MS(500), (e) NiCu/MS(600), (f) NiCu/MS(700), and (g) NiCu/MS(800).

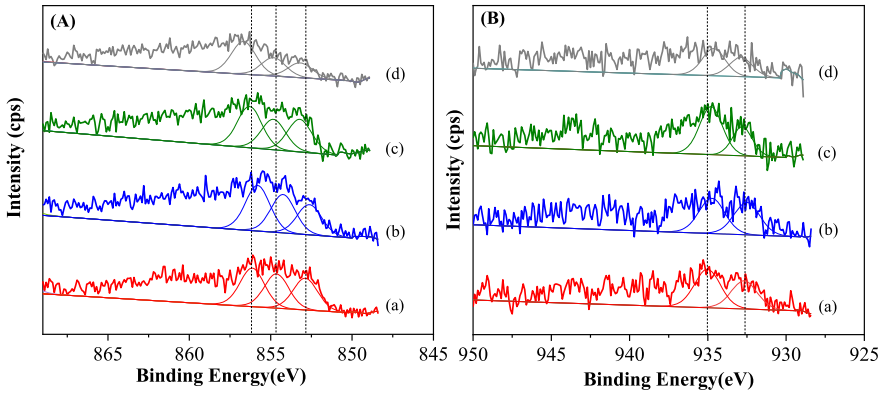

Figure 5. XPS narrow-scan spectra of (A) Ni $2p_{3/2}$ and (B) Cu $2p_{3/2}$ regions of reduced NiCu/MS(x) catalysts. (a) NiCu/MS(500), (b) NiCu/MS(600), (c) NiCu/MS(700), and (d) NiCu/MS(800).

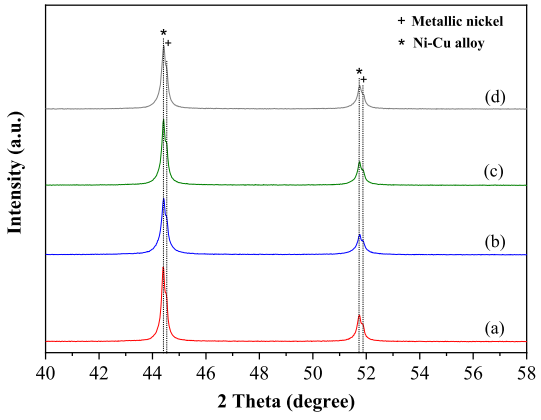

Figure 6. XRD patterns of reduced NiCu/MS(x) catalysts. (a) NiCu/MS(500), (b) NiCu/MS(600), (c) NiCu/MS(700), and (d) NiCu/MS(800).

Table 2. The weight loss curves of the NiCu/MS(500), NiCu/MS(600), NiCu/MS(700), and NiCu/MS(800) catalysts were in the ranges 400−665, 400−690, 400−680, and 400−730 °C, respectively (Figure S3), which corresponded to the decomposition of carbon nanofibers (CNFs).[44] The decomposition temperatures of the CNFs on NiCu/MS(x) catalysts at a higher calcination temperature shifted higher because a stronger CNF structure formed on the NiCu catalyst. The NiCu/MS(600) catalyst had the highest amount of carbon that was 1.02, 1.03, and 1.34 times higher than for NiCu/MS(700), NiCu/MS(800), and NiCu/MS(500) catalysts, respectively.

The turnover frequency (TOF) at the initial reaction time was calculated to evaluate the catalytic activity based on the amount of active nickel metal, and the results are shown in Table 2. The NiCu/MS(800) catalyst had the highest TOF value among all the catalysts that was approximately 1.4, 2.2, and 5.7 times higher than those of the NiCu/MS(700), NiCu/MS(600), and NiCu/MS(500) catalysts, respectively. Considering catalyst stability in terms of the deactivation rate calculated from the CH_4 reaction rate at 180 min of reaction time compared to that at 60 min (Table 2), a value less than one indicates that the catalyst is unstable, whereas a value greater than or equal to one indicates catalyst stability. The deactivation rates of the NiCu/MS(800) and NiCu/MS(500) catalysts were lower than one, indicating that both catalysts were continuously deactivated during the reaction. The results indicated that the NiCu/MS(800) catalyst had outstanding activity initially but its stability was quite poor. In contrast, the

https://doi.org/10.1021/acsomega.2c01016
ACS Omega 2022, 7, 14264−14275

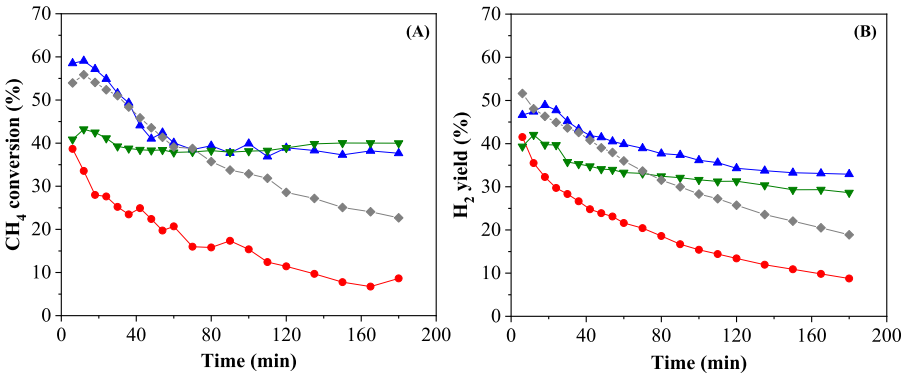

Figure 7. (A) CH_4 conversion and (B) H_2 yield of the NiCu/MS(x) catalyst calcined at different temperatures in methane decomposition at 600 °C. ● (red) NiCu/MS(500), ▲ (blue) NiCu/MS(600), ▼ (green) NiCu/MS(700), and ♦ (gray) NiCu/MS(800).

Table 2. Amounts of Carbon, TOF, Deactivation Rate of Catalysts in the CH_4 Decomposition Reaction, Intensity Ratio of D and G Bands, and Metallic Ni Crystallite Size of Used Catalysts

catalyst	amount of carbon[a] (%)	TOF[b] (1/s)	deactivation rate[c]	I_D/I_G[d]	metallic Ni crystallite size[e] (nm)
NiCu/MS(500)	61.59	24.88	0.415	1.18	33.21
NiCu/MS(600)	82.25	65.30	0.947	1.43	22.98
NiCu/MS(700)	80.31	97.81	1.056	2.05	27.16
NiCu/MS(800)	79.86	141.53	0.562	1.52	28.01

[a]Calculated from TGA data based on weights of the used NiCu/MS(x) catalysts. [b]Calculated as TOF (1/s) at initial reaction time = (% conversion × molar flow rate of CH_4 inlet)/(100 × mole of active nickel). [c]Calculated from the reaction rate of CH_4 at the time on stream of 180 min compared to that of 60 min. [d]Calculated from the Raman data. [e]Calculated from the Scherrer equation.

NiCu/MS(700) and NiCu/MS(600) catalysts had moderate TOF values, but the activities of both catalysts were quite stable during the reaction—the deactivation value of the NiCu/MS(700) catalyst was more than one, while the deactivation value of NiCu/MS(600) catalyst was almost equal to one. The phenomenon of catalyst deactivation is caused by the carbon product formation covering the active nickel metal and the nickel−metal sintering effect, which are discussed later.

2.3. Carbon Allotrope on NiCu/MS(x) Catalysts. The carbon allotrope on the NiCu/MS(x) catalysts used in this study after the CH_4 decomposition reaction at 600 °C was characterized using TEM, Raman spectroscopy, and C1s XPS measurement. As shown in the TEM image in Figure 8, CNFs with different structures formed on the NiCu/MS(x) catalysts synthesized at different calcination temperatures. Fishbone CNFs with average diameters in the range 30−60 nm formed on the NiCu/MS(500) catalyst, whereas mixed fishbone and platelet CNF structures formed on the NiCu/MS(600), NiCu/MS(700), and NiCu/MS(800) catalysts. The average diameters of the fishbone and platelet CNFs of NiCu/MS(600), NiCu/MS(700), and NiCu/MS(800) catalysts were 20−30, 10−30, and 20−40 nm, respectively. The diameter of CNFs depended on the size of Ni and Cu particles because the CNFs formed at the active metal located on the MS support.

Most CNFs formed on the NiCu/MS(500) and NiCu/MS(800) catalysts through the base-growth mechanism, where the active Ni−Cu metals were partially covered by CNFs,[22,36] arising from a strong interaction between Ni−Cu and the MS support (in accordance with the H_2-TPR results). Therefore, the activity and stability of both catalysts were deactivated during the reaction. The fishbone and platelet CNFs on the NiCu/MS(600) and NiCu/MS(700) catalysts were mostly formed through the tip-growth mechanism, where the active sites of nickel−copper were on the tips of the CNFs,[22,36] resulting from a weak interaction between Ni−Cu on the MS support (H_2-TPR results; Figure 2). This phenomenon resulted in higher catalyst activity and prolonged catalyst stability during the reaction. The metal particle shape and the interface between the metal and support directly affected the formation of the CNF structures. With the fishbone CNF formation, with the metal particles having a rhombic morphology or polygonal cluster, the carbon was precipitated from a faceted catalyst particle to generate a structure in which the graphitic platelets were aligned at an angle to the fiber axis.[45,46] For platelet CNF formation, the graphite platelets were stacked in a direction parallel to the base of the metal particle and perpendicular to the fiber axis via the tip-growth mechanism.[47,48]

Considering the MS pore structure after the reaction, Figure S2b,d focused on the support structure. It was found that the MS support was covered by carbon, with the mesocellular structure (foam-like structure) of the NiCu/MS(x) catalyst not changing during the reaction.

Raman spectra of the used NiCu/MS(x) catalysts obtained from the different calcination temperatures are shown in Figure 9. The positions were observed in the used NiCu/MS(x) catalysts of the D band at 1330 cm^{-1} and the G band at 1575 cm^{-1}, corresponding to scattering from structural defects or disorders in the carbon and the in-plane vibrations of the carbon atom sp^2 hybridization in the graphitic structure, respectively.[49,50] The higher intensity ratio of the D and G bands of the NiCu/MS(700) catalyst compared to the other catalyst clearly depicted the defective nature of the platelet carbon nanofibers. The lowest intensity ratio of the D and G bands was found in the NiCu/MS(500) catalyst, indicating a higher crystalline structure of the fishbone CNFs. The alignment and crystalline perfection of the platelets and fishbones were related to the nature and shape of the metal catalyst particle and the orientation of the precipitating faces.

https://doi.org/10.1021/acsomega.2c01016
ACS Omega 2022, 7, 14264−14275

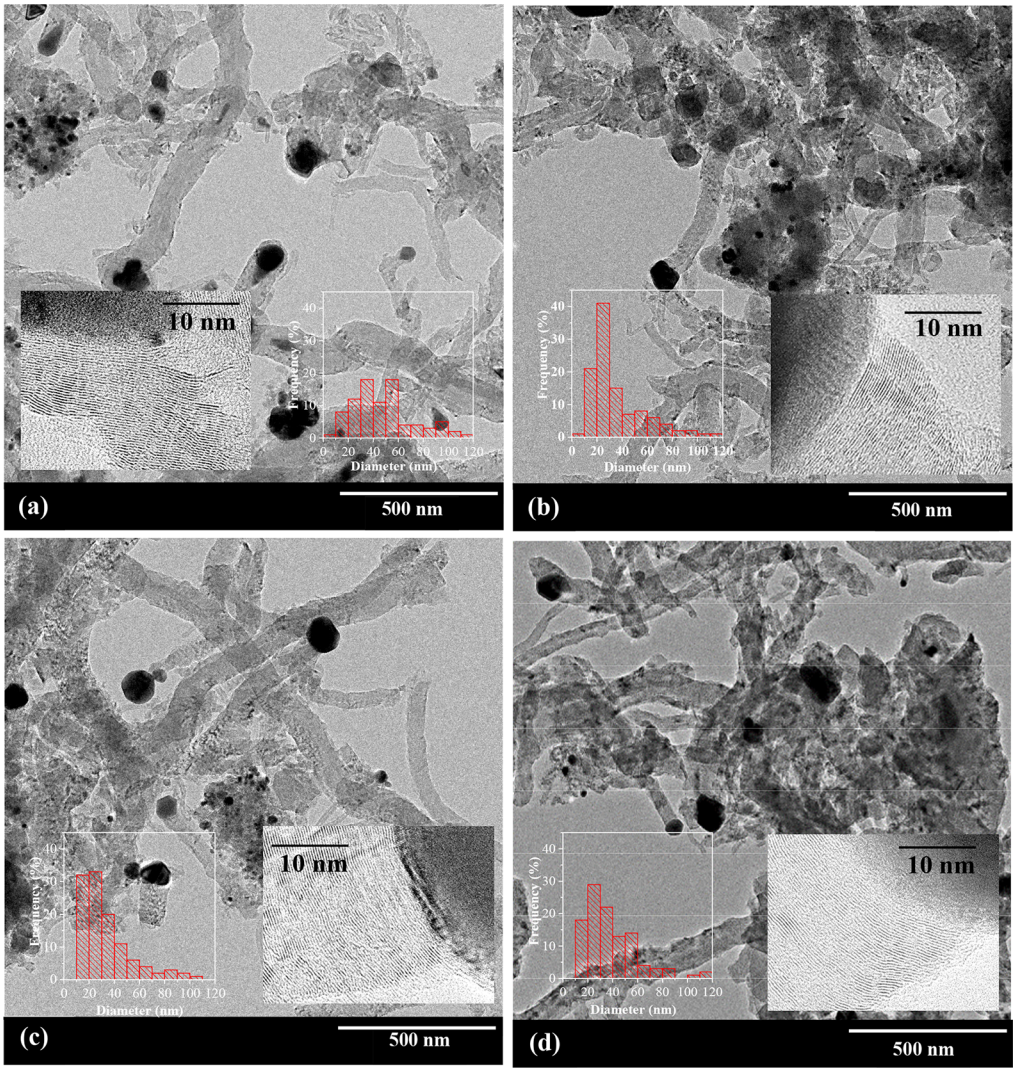

Figure 8. TEM image and histograms of CNF diameter distributions of used NiCu/MS(x) catalysts after the CH_4 decomposition reaction. (a) NiCu/MS(500), (b) NiCu/MS(600), (c) NiCu/MS(700), and (d) NiCu/MS(800).

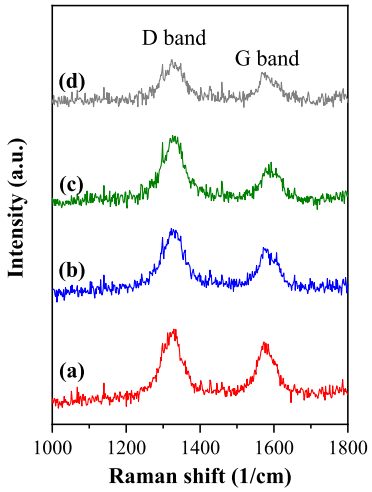

Figure 9. Raman spectra of used NiCu/MS(x) catalysts after the CH_4 decomposition reaction. (a) NiCu/MS(500), (b) NiCu/MS(600), (c) NiCu/MS(700), and (d) NiCu/MS(800).

To clarify the carbon bonding, the used NiCu/MS(x) catalysts after the CH_4 decomposition reaction were examined using the XPS measurement, and the binding energy region of the C 1s core level is shown in Figure S4. All the used catalysts had similar C 1s peak deconvoluted into five peaks at 284.2 ± 0.1, 284.9 ± 0.1, 285.6 ± 0.2, 286.4 ± 0.2, and 287.4 ± 0.3 eV, which corresponded to metal carbide, sp^2 carbon, sp^3 carbon, carbonyl groups (C−O), and carboxyl groups (C═O),[49,51,52] respectively. The two main peaks of sp^2 carbon and sp^3 carbon were associated with sp^2 and sp^3 hybridization of the C−C or C−H bonds in the graphite structure of the CNFs formed on the used catalyst. The relative intensity ratio of sp^2 carbon and sp^3 carbon of used catalysts is presented in Table 3. The lowest intensity ratio of sp2 and sp3 carbons was for the NiCu/MS(600) catalyst, resulting from a higher proportion of sp3 hybridization in the structure.

2.4. Characterization of Used NiCu/MS(x) Catalysts.

Figure 10 shows the XRD pattern of the used NiCu/MS(x) catalysts after the CH_4 decomposition reaction at 600 °C. The diffraction patterns at 2θ of 26.3°, 42.8°, and 54.1° indexed as the (002), (10), and (11) graphite-type reflections[50] were found in all the used NiCu/MS(x) catalysts. Considering the metal catalyst, the diffraction peaks at 2θ of 44.42° and 51.76° were assigned to the Ni−Cu alloy (JCPDS. 47-1406), and the shoulders peak located at 2θ of 44.51° and 51.92°

https://doi.org/10.1021/acsomega.2c01016
ACS Omega 2022, 7, 14264−14275

Table 3. Binding Energy and Fitting Results of C 1s XPS Spectra of Used NiCu/MS(x) Catalysts after CH_4 Decomposition Reaction

catalyst	metal carbide (%)	sp^2-carbon (%)	sp^3-carbon (%)	C−O (%)	C=O (%)	sp^2/sp^3
NiCu/MS(500)	284.2 (3.2)	284.9 (63.9)	285.6 (15.7)	286.4 (10.0)	287.4 (7.2)	4.07
NiCu/MS(600)	284.3 (3.6)	284.9 (56.2)	285.6 (22.9)	286.5 (10.5)	287.5 (6.8)	2.45
NiCu/MS(700)	284.1 (2.3)	285.1 (60.6)	285.8 (16.5)	286.6 (13.6)	287.7 (7.1)	3.67
NiCu/MS(800)	284.2 (2.4)	284.9 (67.6)	285.6 (15.2)	286.4 (8.8)	287.3 (5.9)	4.45

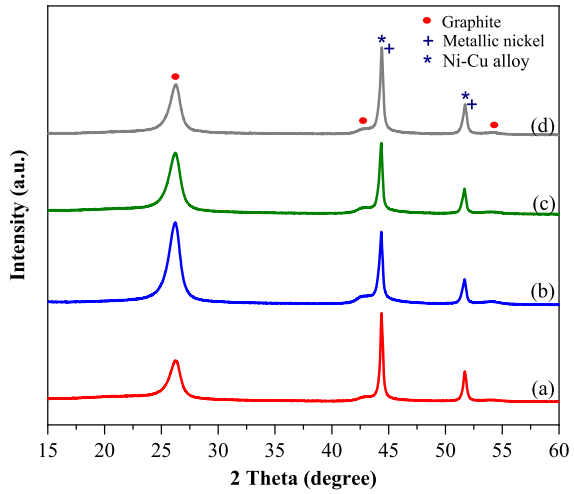

Figure 10. XRD patterns of used NiCu/MS(x) catalysts after the CH_4 decomposition reaction. (a) NiCu/MS(500), (b) NiCu/MS(600), (c) NiCu/MS(700), and (d) NiCu/MS(800).

corresponded to the metallic nickel (JCPDS. 4-0850).[14,42,43] However, the diffraction peak of copper was not identified in the used catalysts because the copper metal was well dispersed on the catalyst surface.

The crystallite sizes of the metallic nickel of the used catalysts calculated using the Scherrer equation are presented in Table 2. The smallest and largest metallic nickel crystallite sizes were in the used NiCu/MS(600) and NiCu/MS(500) catalysts, respectively. In addition, the crystallite sizes of the metallic nickel of the used catalysts were smaller than those of the fresh catalysts. Comparing the fresh and used NiCu/MS(x) catalysts, the decreasing metallic Ni crystallite sizes of NiCu/MS(500), NiCu/MS(600), NiCu/MS(700), and NiCu/MS(800) were 16.55, 35.08, 30.54, and 23.47%, respectively. Among them, the Ni crystallite size of the NiCu/MS(600) catalyst significantly decreased after the reaction. This could be explained by the addition of Cu in the NiCu/MS catalyst promoting fragmentation of the parent Ni−Cu particles when in contact with hydrocarbons.[47] Furthermore, the Cu-modified Ni-supported mesocellular silica catalyst calcined at 600 °C resulted in the interaction between Ni and the MS support becoming weaker due to selective Ni fragmentation when the methane molecule decomposed into carbon species and simultaneously formed CNFs through the tip-growth mechanism on the catalyst surface (as shown in Figure 8). Accordingly, the activity of the NiCu/MS(600) catalyst was quite high and stable during the reaction.

3. CONCLUSIONS

Cu-modified Ni-supported mesocellular silica [NiCu/MS(x)] catalysts were synthesized using the co-impregnation method, focusing on the role of the calcination temperature in determining hydrogen production and carbon allotropes during the catalytic CH_4 decomposition reaction. The results showed that the nickel and copper reduction behaviors of the NiCu/MS(600) catalyst occurred at lower temperature, indicating a weaker interaction in the NiCu−MS support compared to the other catalysts. With the increase in calcination temperature, the NiCu−MS support interaction of the NiCu/MS(x) catalysts became stronger. Regarding catalyst performance, the maximum CH_4 conversion and H_2 yield occurred with the NiCu-supported mesocellular silica catalyst, with an optimum calcination temperature of 600 °C. Furthermore, the activity of the NiCu/MS(600) catalyst was stable during the reaction, perhaps due to the high number of active nickel sites and the weak interaction between nickel−copper and the MS support selectively forming fishbone and platelet carbon nanofibers via a tip-growth mechanism. In contrast, the activities of the NiCu/MS(500) and NiCu/MS(800) catalysts significantly decreased with the increase in reaction time because of their strong interaction between NiCu and the MS support, resulting in active NiCu sites being covered by the selective CNF formation via the based-growth mechanism.

4. EXPERIMENTAL SECTION

4.1. Catalyst Preparation. The bimetallic Ni−Cu loaded on the mesocellular silica (NiCu/MS) catalyst with different calcination temperatures was prepared using two steps: mesocellular silica synthesis and a bimetallic loading step. The mesocellular silica (MS) synthesis was synthesized using the sol−gel process with sodium silicate (29.45% silica; C. Thai Chemical Company) as the silica source, Pluronic P123 as the pore structure agent and 1,3,5-trimethylbenzene (TMB) as the swelling agent. First, Pluronic P123 was dissolved in deionized water under stirring at room temperature until the solution was clear. After that, hydrochloric acid (37 wt.%) and TMB (TMB and Pluronic P123 at a weight ratio of 2:1) were consecutively added into the Pluronic P123 solution while stirring at 40 °C. Then, the sodium silicate was dropped into the solution and stirring continued at 40 °C for 24 h. The mixed solution was hydrothermally treated in an autoclave at 100 °C for 24 h. The obtained product was filtered and washed with deionized water, dried at 100 °C overnight, and calcined in air at 550 °C for 6 h.

For the bimetallic loading process, amounts of 50 wt % nickel (Ni) and 5 wt % copper (Cu) were loaded onto the MS support using the incipient wetness co-impregnation method. Nickel nitrate [$Ni(NO_3)_2{\cdot}6H_2O$] and copper nitrate [$Cu(NO_3)_2{\cdot}3H_2O$] were dissolved in deionized water. Then, the nickel−copper solution was dropped into the MS support while stirring at room temperature for 1 h. After that, the mixture was dried in a microwave oven at 800 W for 1 min, before being calcined at different temperatures (500, 600, 700, and 800 °C) for 4 h. The catalysts were denoted as NiCu/MS(x), where x is the calcination temperature of the catalyst.

https://doi.org/10.1021/acsomega.2c01016
ACS Omega 2022, 7, 14264−14275

4.2. Catalyst Characterization. The textural properties of the NiCu/MS(x) catalysts were examined using N_2 physisorption with a 3 Flex Surface Characterization Analyzer. The surface area and pore size distributions were calculated using the Brunauer–Emmett–Teller (BET) and Barrett–Joyner–Halenda (BJH) methods under relative pressure (P/P_0) at −196 °C. Specific pore volume was obtained at a relative pressure of 0.995.

The structure of fresh NiCu/MS(x) and carbon product on the used NiCu/MS(x) catalysts were observed using transmission electron microscopy (TEM: JEOL JEM2010 instrument) with an acceleration voltage of 200 kV.

The reduction temperature and interaction between nickel, copper, and the MS support were identified using the hydrogen temperature-programmed reduction (H_2-TPR) technique (Micromeritics, Autochem II Chemisorption analyzer). During the process, an H_2/Ar gas mixture (10% H_2, Ar balance) was introduced into the catalyst bed at a total flow rate of 50 ml/min at room temperature; the temperature was increased to 1000 °C using a heating rate of 5 °C/min. The amount of H_2 consumption was analyzed using a thermal conductivity detector (TCD).

Nickel and copper species were examined by X-ray absorption near edge structure (XANES) measurements using time-resolved X-ray absorption spectroscopy (TR-XAS) at Beamline 2.2 of the Synchrotron Light Research Institute (SLRI), Thailand. The beamline uses an energy-dispersive monochromator equipped with a Si (1 1 1) single crystal.

The chemical states and surface atomic concentrations of the reduced and used NiCu/MS(x) catalysts were analyzed using X-ray photoelectron spectroscopy (XPS: AXIS Ultra DLD). The C 1s peak at 284.8 eV was applied as a reference peak to calibrate the binding energy.

The crystalline structures of reduced NiCu/MS(x) catalysts were examined by using X-ray diffraction spectroscopy (Bruker D8 Advance) operated with monochromated Cu Kα radiation (40 kV and 40 mA) in the 2θ range of 10°–70°.

The active Ni surface area on the catalyst was determined by using the CO chemisorption technique (Micromeritics: Autochem II Chemisorption analyzer). Prior to chemisorption analysis, the catalyst was activated under H_2 flow at 700 °C for 1.5 h. The CO chemisorption was operated at 50 °C by pulse-dosing. The amount of CO adsorbed on the catalyst was monitored by using TCD.

The amount and type of carbon product formed on the NiCu/MS(x) catalysts after the methane decomposition reaction were investigated using a thermogravimetric analysis (TGA) technique (METTLER TOLEDO, TGA/DSC 3+) from 30 to 800 °C at a heating rate of 5 °C/min in air flow.

The crystallinity of the carbon formed on the used NiCu/MS(x) catalyst was characterized using Raman spectroscopy (NTEGRA spectra, NT-MDT) with a laser wavelength of 632.8 nm.

4.3. Catalytic Activity Test. The effect of calcination temperature on the NiCu/MS(x) catalysts in the methane decomposition reaction was investigated using a packed-bed reactor. In the experiment, 0.1 g of catalyst was packed in an Inconel tube reactor (Inconel-600, O.D. 3/8″) in the center of a tubular furnace equipped with a K-type thermocouple. The catalyst was activated using H_2 gas at a flow rate of 60 mL/min at 700 °C for 1.5 h. In the methane decomposition reaction, CH_4 and N_2 reactant gases (volume ratio of 1:9) with a total flow rate of 100 mL/min [a gas hourly space velocity (GHSV) of 60,000 mL/h·$g_{catalyst}$] were fed into the reactor. The reaction temperature was operated at 600 °C under atmospheric pressure. During the reaction, the remaining reactants and products were analyzed using a Shimadzu gas chromatograph (GC14A) equipped with TCD and using a Unibead-C packed column for H_2, CO, CH_4, and CO_2 analysis using Ar as a carrier gas.

■ ASSOCIATED CONTENT

Supporting Information

The Supporting Information is available free of charge at https://pubs.acs.org/doi/10.1021/acsomega.2c01016.

Nitrogen adsorption–desorption isotherms and pore size distributions of fresh NiCu/MS(x) catalysts: NiCu/MS(500), NiCu/MS(600), NiCu/MS(700), and NiCu/MS(800); TEM image of fresh NiCu/MS(500), used NiCu/MS(500), fresh NiCu/MS(600), and used NiCu(600) catalysts; weight loss curve of used NiCu/MS(x) catalysts after CH_4 decomposition reaction; and XPS narrow-scan spectra of C 1s core level of used NiCu/MS(x) catalysts: NiCu/MS(500), NiCu/MS(600), NiCu/MS(700), and NiCu/MS(800) (PDF)

■ AUTHOR INFORMATION

Corresponding Author

Waleeporn Donphai − *KU-Green Catalysts Group, Department of Chemical Engineering, Faculty of Engineering, Kasetsart University, Bangkok 10900, Thailand; Research Network of NANOTEC—KU on NanoCatalysts and NanoMaterials for Sustainable Energy and Environment, Kasetsart University, Bangkok 10900, Thailand;* orcid.org/0000-0002-9422-638X; Email: fengwod@ku.ac.th

Authors

Orrakanya Phichairatanaphong − *KU-Green Catalysts Group, Department of Chemical Engineering, Faculty of Engineering, Kasetsart University, Bangkok 10900, Thailand*

Yingyot Poo-Arporn − *Synchrotron Light Research Institute, Nakhon Ratchasima 30000, Thailand*

Metta Chareonpanich − *KU-Green Catalysts Group, Department of Chemical Engineering, Faculty of Engineering, Kasetsart University, Bangkok 10900, Thailand; Research Network of NANOTEC—KU on NanoCatalysts and NanoMaterials for Sustainable Energy and Environment, Kasetsart University, Bangkok 10900, Thailand;* orcid.org/0000-0002-4333-337X

Complete contact information is available at: https://pubs.acs.org/10.1021/acsomega.2c01016

Notes

The authors declare no competing financial interest.

■ ACKNOWLEDGMENTS

This work was financially supported by the Office of the Permanent Secretary, Ministry of Higher Education, Science, Research and Innovation (RGNS 63-039), the Research Network of NANOTEC (RNN), the Ministry of Science and Technology, Thailand, the Center for Advanced Studies in Nanotechnology for Chemical, Food and Agricultural Industries, Kasetsart University, the Kasetsart University Research

and Development Institute (KURDI), the Faculty of Engineering, Kasetsart University, and the Center of Excellence on Petrochemical and Materials Technology (PETROMAT). The authors would like to thank the Synchrotron Light Research Institute for support with XAS (BL 2.2: TR-XAS) measurement.

REFERENCES

(1) Amikam, G.; Fridman-Bishop, N.; Gendel, Y. Biochar-assisted iron-mediated water electrolysis process for hydrogen production. *ACS Omega* **2020**, *5*, 31908−31917.
(2) Wang, D.; Zhang, J.; Sun, J.; Gao, W.; Cui, Y. Effect of metal additives on the catalytic performance of Ni/Al_2O_3 catalyst in thermocatalytic decomposition of methane. *Int. J. Hydrogen Energy* **2019**, *44*, 7205−7215.
(3) Ashik, U. P. M.; Wan Daud, W. M. A.; Hayashi, J.-i. A review on methane transformation to hydrogen and nanocarbon: Relevance of catalyst characteristics and experimental parameters on yield. *Renew. Sustain. Energy Rev.* **2017**, *76*, 743−767.
(4) Chaubey, R.; Sahu, S.; James, O. O.; Maity, S. A review on development of industrial processes and emerging techniques for production of hydrogen from renewable and sustainable sources. *Renew. Sustain. Energy Rev.* **2013**, *23*, 443−462.
(5) Sun, H.; Yang, Z.; Shi, G.; Arhin, S. G.; Papadakis, V. G.; Goula, M. A.; Zhou, L.; Zhang, Y.; Liu, G.; Wang, W. Methane production from acetate, formate and H_2/CO_2 under high ammonia level: Modified ADM1 simulation and microbial characterization. *Sci. Total Environ.* **2021**, *783*, 147581.
(6) Arevalo, R. L.; Aspera, S. M.; Sison Escaño, M. C.; Nakanishi, H.; Kasai, H. Ru-catalyzed steam methane reforming: mechanistic study from first principles calculations. *ACS Omega* **2017**, *2*, 1295−1301.
(7) Kim, J.; Ryou, Y.; Kim, T. H.; Hwang, G.; Bang, J.; Jung, J.; Bang, Y.; Kim, D. H. Highly selective production of syngas (>99%) in the partial oxidation of methane at 480°C over Pd/CeO_2 catalyst promoted by HCl. *Appl. Surf. Sci.* **2021**, *560*, 150043.
(8) Avraam, D. G.; Halkides, T. I.; Liguras, D. K.; Bereketidou, O. A.; Goula, M. A. An experimental and theoretical approach for the biogas steam reforming reaction. *Int. J. Hydrogen Energy* **2010**, *35*, 9818−9827.
(9) Luo, H.; Qiao, Y.; Ning, Z.; Bo, C.; Hu, J. Effect of Thermal Extraction on Coal-Based Activated Carbon for Methane Decomposition to Hydrogen. *ACS Omega* **2020**, *5*, 2465−2472.
(10) Hasnan, N. S. N.; Timmiati, S. N.; Pudukudy, M.; Yaakob, Z.; Lim, K. L.; Taufiq-Yap, Y. H. Catalytic decomposition of methane into hydrogen and carbon nanotubes over mesostructured silica nanoparticle-supported nickel catalysts. *J. Porous Mater.* **2020**, *27*, 369−382.
(11) Mahmoodzade, E.; Meshkani, F.; Rezaei, M.; Rastegarpanah, A. Preparation and improvement of nickel catalyst supported ordered mesoporous spherical silica for thermocatalytic decomposition of methane. *J. Energy Inst.* **2020**, *93*, 2488−2496.
(12) Dipu, A. L. Methane decomposition into COx-free hydrogen over a Ni-based catalyst: An overview. *Int. J. Energy Res.* **2021**, *45*, 9858−9877.
(13) Gamal, A.; Eid, K.; El-Naas, M. H.; Kumar, D.; Kumar, A. Catalytic Methane Decomposition to Carbon Nanostructures and COx-Free Hydrogen: A Mini-Review. *Nanomaterials* **2021**, *11*, 1226.
(14) Donphai, W.; Witoon, T.; Faungnawakij, K.; Chareonpanich, M. Carbon-structure Affecting Catalytic Carbon Dioxide Reforming of Methane Reaction over Ni-carbon Composites. *J. CO_2 Util.* **2016**, *16*, 245−256.
(15) Han, Y.-J.; Park, S.-J. Influence of nickel nanoparticles on hydrogen storage behaviors of MWCNTs. *Appl. Surf. Sci.* **2017**, *415*, 85−89.
(16) Malik, R.; Zhang, L.; McConnell, C.; Schott, M.; Hsieh, Y.-Y.; Noga, R.; Alvarez, N. T.; Shanov, V. Three-dimensional, free-standing polyaniline/carbon nanotube composite-based electrode for high-performance supercapacitors. *Carbon* **2017**, *116*, 579−590.
(17) Rategarpanah, A.; Meshkani, F.; Wang, Y.; Arandiyan, H.; Rezaei, M. Thermocatalytic conversion of methane to highly pure hydrogen over $Ni-Cu/MgO{\cdot}Al_2O_3$ catalysts: Influence of noble metals (Pt and Pd) on the catalytic activity and stability. *Energy Convers. Manag.* **2018**, *166*, 268−280.
(18) Echegoyen, Y.; Suelves, I.; Lázaro, M. J.; Sanjuán, M. L.; Moliner, R. Thermo catalytic decomposition of methane over Ni−Mg and Ni−Cu−Mg catalysts: Effect of catalyst preparation method. *Appl. Catal., A* **2007**, *333*, 229−237.
(19) Panchan, N.; Donphai, W.; Junsomboon, J.; Niamnuy, C.; Chareonpanich, M. Influence of the calcination technique of silica on the properties and performance of Ni/SiO_2 catalysts for synthesis of hydrogen via methane cracking reaction. *ACS Omega* **2019**, *4*, 18076−18086.
(20) Gutta, N.; Velisoju, V. K.; Chatla, A.; Boosa, V.; Tardio, J.; Patel, J.; Akula, V. Promotional Effect of Cu and Influence of Surface Ni−Cu Alloy for Enhanced H_2 Yields from CH_4 Decomposition over Cu-Modified Ni Supported on MCM-41 Catalyst. *Energy Fuels* **2018**, *32*, 4008−4015.
(21) Qian, J. X.; Chen, T. W.; Enakonda, L. R.; Liu, D. B.; Mignani, G.; Basset, J.-M.; Zhou, L. Methane decomposition to produce COx-free hydrogen and nano-carbon over metal catalysts: A review. *Int. J. Hydrogen Energy* **2020**, *45*, 7981−8001.
(22) Phichairatanaphong, O.; Teepakakorn, P.; Poo-arporn, Y.; Chareonpanich, M.; Donphai, W. Infiltrate mesoporous silica-aluminosilicate structure improves hydrogen production via methane decomposition over a nickel-based catalyst. *Ind. Eng. Chem. Res.* **2021**, *60*, 4562−4574.
(23) Charisiou, N. D.; Papageridis, K. N.; Siakavelas, G.; Sebastian, V.; Hinder, S. J.; Baker, M. A.; Polychronopoulou, K.; Goula, M. A. The influence of SiO_2 doping on the Ni/ZrO_2 supported catalyst for hydrogen production through the glycerol steam reforming reaction. *Catal. Today* **2019**, *319*, 206−219.
(24) Rastegarpanah, A.; Rezaei, M.; Meshkani, F.; Dai, H.; Arandiyan, H. Thermocatalytic decomposition of methane over mesoporous $Ni/xMgO{\cdot}Al_2O_3$ nanocatalysts. *Int. J. Hydrogen Energy* **2018**, *43*, 15112−15123.
(25) Keller, M.; Sharma, A. Hydrogen production via methane cracking on dry-coated Fe/ZrO_2 with support recycle in a fluidized bed process. *Energy Fuels* **2021**, *35*, 847−855.
(26) Tanggarnjanavalukul, C.; Donphai, W.; Witoon, T.; Chareonpanich, M.; Limtrakul, J. Deactivation of nickel catalysts in methane cracking reaction: Effect of bimodal meso-macropore structure of silica support. *Chem. Eng. J.* **2015**, *262*, 364−371.
(27) Widyaningrum, R. N.; Church, T. L.; Zhao, M.; Harris, A. T. Mesocellular-foam-silica-supported Ni catalyst: Effect of pore size on H_2 production from cellulose pyrolysis. *Int. J. Hydrogen Energy* **2012**, *37*, 9590−9601.
(28) Qian, L.; Lv, X.; Ren, Y.; Wang, H.; Chen, G.; Wang, Y.; Shen, J. Inverse gas chromatography applied in the surface properties evaluation of mesocellular silica foams modified by sized nickel nanoparticles. *J. Chromatogr. A* **2013**, *1322*, 81−89.
(29) Fakeeha, A. H.; Al Fatesh, A. S.; Ibrahim, A. A.; Kurdi, A. N.; Abasaeed, A. E. Yttria modified ZrO_2 supported Ni catalysts for CO_2 reforming of methane: The role of Ce promoter. *ACS Omega* **2021**, *6*, 1280−1288.
(30) Torres, D.; Pinilla, J. L.; Suelves, I. Screening of Ni-Cu bimetallic catalysts for hydrogen and carbon nanofilaments production via catalytic decomposition of methane. *Appl. Catal., A* **2018**, *559*, 10−19.
(31) Shen, Y.; Ge, M.; Lua, A. C. Deactivation of bimetallic nickel-copper alloy catalyst in thermocatalytic decomposition of methane. *Catal. Sci. Technol.* **2018**, *8*, 3853−3862.
(32) Awad, A.; Masiran, N.; Abdus Salam, M.; Vo, D.-V. N.; Abdullah, B. Non-oxidative decomposition of methane/methanol mixture over mesoporous $Ni-Cu/Al_2O_3$ Co-doped catalysts. *Int. J. Hydrogen Energy* **2019**, *44*, 20889−20899.

https://doi.org/10.1021/acsomega.2c01016
ACS Omega 2022, 7, 14264−14275

(33) Saraswat, S. K.; Pant, K. K. Synthesis of hydrogen and carbon nanotubes over copper promoted Ni/SiO_2 catalyst by thermocatalytic decomposition of methane. *J. Nat. Gas Sci. Eng.* **2013**, *13*, 52−59.
(34) Cychosz, K. A.; Thommes, M. Progress in the physisorption characterization of nanoporous gas storage materials. *Engineering* **2018**, *4*, 559−566.
(35) Qian, L.; Cai, W.; Zhang, L.; Ye, L.; Li, J.; Tang, M.; Yue, B.; He, H. The promotion effect of hydrogen spillover on CH_4 reforming with CO_2 over Rh/MCF catalysts. *Appl. Catal., B* **2015**, *164*, 168−175.
(36) Donphai, W.; Phichairatanaphong, O.; Klysubun, W.; Chareonpanich, M. Hydrogen and carbon allotrope production through methane cracking over Ni/bimodal porous silica catalyst: Effect of nickel precursor. *Int. J. Hydrogen Energy* **2018**, *43*, 21798−21809.
(37) Fedorov, A. V.; Kukushkin, R. G.; Yeletsky, P. M.; Bulavchenko, O. A.; Chesalov, Y. A.; Yakovlev, V. A. Temperature-programmed reduction of model CuO, NiO and mixed CuO−NiO catalysts with hydrogen. *J. Alloys Compd.* **2020**, *844*, 156135.
(38) Salunkhe, P.; A v, M. A.; Kekuda, D. Investigation on tailoring physical properties of Nickel Oxide thin films grown by dc magnetron sputtering. *Mater. Res. Express* **2020**, *7*, 016427.
(39) Dubey, P.; Kaurav, N.; Devan, R. S.; Okram, G. S.; Kuo, Y. K. The effect of stoichiometry on the structural, thermal and electronic properties of thermally decomposed nickel oxide. *RSC Adv.* **2018**, *8*, 5882−5890.
(40) Hiraba, H.; Koizumi, H.; Kodaira, A.; Takehana, K.; Yoneyama, T.; Matsumura, H. Effects of copper surface oxidation and reduction on shear-bond strength using functional monomers. *Materials* **2021**, *14*, 1753.
(41) Pauly, N.; Tougaard, S.; Yubero, F. Determination of the Cu 2p primary excitation spectra for Cu, Cu_2O and CuO. *Surf. Sci.* **2014**, *620*, 17−22.
(42) Naghash, A. R.; Etsell, T. H.; Xu, S. XRD and XPS study of Cu-Ni interactions on reduced Copper-Nickel-Aluminum oxide solid solution catalysts. *Chem. Mater.* **2006**, *18*, 2480−2488.
(43) Ge, Y.; Ma, Y.; Xue, R.; Wang, F.; Su, P.; Wang, Z.; Li, Y. CeO_2- and CaO-promoted precipitation method for one-step preparation of vermiculite-based multilayer mesoporous Ni-based catalysts for dry reforming of methane. *ACS Omega* **2021**, *6*, 17019−17026.
(44) Romero, A.; Garrido, A.; Nieto-Márquez, A.; de la Osa, A. R.; de Lucas, A.; Valverde, J. L. The influence of operating conditions on the growth of carbon nanofibers on carbon nanofiber-supported nickel catalysts. *Appl. Catal., A* **2007**, *319*, 246−258.
(45) Terrones, H.; Hayashi, T.; Muñoz-Navia, M.; Terrones, M.; Kim, Y. A.; Grobert, N.; Kamalakaran, R.; Dorantes-Dávila, J.; Escudero, R.; Dresselhaus, M. S.; Endo, M. Graphitic cones in palladium catalysed carbon nanofibers. *Chem. Phys. Lett.* **2001**, *343*, 241−250.
(46) Ruiz-Cornejo, J. C.; Sebastián, D.; Lázaro, M. J. Synthesis and applications of carbon nanofibers: A review. *Rev. Chem. Eng.* **2020**, *36*, 493−511.
(47) Zhao, T.; Kvande, I.; Yu, Y.; Ronning, M.; Holmen, A.; Chen, D. Synthesis of platelet carbon nanofiber/carbon felt composite on in situ generated Ni−Cu nanoparticles. *Phys. Chem. C* **2011**, *115*, 1123−1133.
(48) De Jong, K. P.; Geus, J. W. Carbon nanofibers: catalytic synthesis and applications. *Catal. Rev. Sci. Eng.* **2000**, *42*, 481−510.
(49) Varga, M.; Izak, T.; Vretenar, V.; Kozak, H.; Holovsky, J.; Artemenko, A.; Hulman, M.; Skakalova, V.; Lee, D. S.; Kromka, A. Diamond/carbon nanotube composites: Raman, FTIR and XPS spectroscopic studies. *Carbon* **2017**, *111*, 54−61.
(50) Pawlyta, M.; Rouzaud, J.-N.; Duber, S. Raman micro-spectroscopy characterization of carbon blacks: Spectral analysis and structural information. *Carbon* **2015**, *84*, 479−490.
(51) Krasovskii, P. V.; Malinovskaya, O. S.; Samokhin, A. V.; Blagoveshchenskiy, Y. V.; Kazakov, V. A.; Ashmarin, A. A. XPS study of surface chemistry of tungsten carbides nanopowders produced through DC thermal plasma/hydrogen annealing process. *Appl. Surf. Sci.* **2015**, *339*, 46−54.
(52) Cortés-López, A. J.; Muñoz-Sandoval, E.; López-Urías, F. Oxygenated surface of carbon nanotube sponges: Electroactivity and magnetic studies. *ACS Omega* **2019**, *4*, 18011−18022.

https://doi.org/10.1021/acsomega.2c01016
ACS Omega 2022, 7, 14264−14275